Available online at www.sciencedirect.com
ScienceDirect
International Journal of Heat and Mass Transfer 51 (2008) 2889–2904
International Journal of HEAT and MASS TRANSFER
www.elsevier.com/locate/ijhmt

Natural convection in an enclosure with localized heating and salting from below

Fu-Yun Zhao, Di Liu, Guang-Fa Tang *

College of Civil Engineering, Hunan University, Changsha 410082, PR China

Received 6 March 2007; received in revised form 27 June 2007
Available online 20 February 2008

Abstract

Two-dimensional, double diffusion, natural convection in a rectangular enclosure filled with binary fluid saturating porous media is investigated numerically. Multiple motions are driven by the external temperature and concentration differences imposed across horizontal walls with the simultaneous presence of discrete heat and contaminant sources. The general Brinkman-extended Darcy model is adopted to formulate the fluid flow in the cavity. The fluid, heat and moisture transport through the isotropic porous layer are analyzed using the streamlines, heatlines and masslines, and the heat and mass transfer potentials are also explained by the variations of overall Nusselt and Sherwood numbers. The numerical simulations presented here span a wide range of the main parameters (thermal Rayleigh numbers, strip pitches and Darcy number) in the domain of destabilizing solutal buoyancy forces. It is shown that the heat and mass transfer potential can be promoted or inhibited, depending strongly on the permeability of porous medium, the strip pitch, the thermal and solutal Rayleigh numbers.

Keywords: Enclosure flow; Natural convection; Discrete heat source; Heatlines and masslines; Porous medium

1. Introduction

During the past few decades, innumerable theoretical, numerical and experimental studies have dealt with natural convection confined to enclosures completely filled by a fluid or a porous medium. Most recently, the trend in the research community has shifted to the examination of simultaneous heat and mass transfer or double-diffusion convection in enclosures. As expected, this situation is generally more complex than those when each phenomenon acts alone. Double-diffusive natural convection in enclosures has been encountered in many engineering fields, such as oceanography, astrophysics, geology, biology, and chemical processes etc. This fact is amply reflected by the size of the research effort dedicated to this topic [1–3].

The phenomenon of double-diffusive natural convection in an enclosure is as varied as the thermal and solutal boundary conditions, geometry and orientation of the enclosure. Judging from the number of potential engineering applications, the enclosure phenomena can be organized into three classes: (1) double diffusion in an horizontal layer with vertical temperature and concentration gradients [4–6]; (2) thermosolutal natural convection due to horizontal temperature and concentration gradients in vertical enclosures [5,7–19]; (3) sideways heating of an initially stratified fluid layer [20–22]. Their attentions have been given to the convective fluid [4,5,9–12,14,17–22] or porous layers [6–8,13,15,16] that are induced or destabilized by uniform heat (mass) fluxes or uniform higher temperature (concentration).

Other engineering systems, however, may be characterized by double-diffusive behavior driven by thermal and solutal buoyancies induced by discrete heat and mass sources. For example, possible non-uniformities in the release of buoyant element due to heat exchanger leakage

* Corresponding author. Tel.: + 86 731 8822760; fax: + 86 731 8822667.
E-mail addresses: zfycfdnet@163.com (F.-Y. Zhao), liudi66@163.com (D. Liu), gftangcfd@163.com (G.-F. Tang).

0017-9310/$ - see front matter © 2007 Elsevier Ltd. All rights reserved.
doi:10.1016/j.ijheatmasstransfer.2007.09.032

Nomenclature

Ar	cavity aspect ratio (L/H)
D	solutal diffusivity
Da	Darcy number
g	gravitational acceleration
H	height of the enclosure
k	thermal conductivity
K	permeability
L	width of the enclosure
Le	Lewis number
L_{ts}	pitch of the discrete segments
N	buoyancy ratio ($\beta_s\Delta s/\beta_t\Delta t$)
Nu	overall Nusselt number
P	Dimensionless pressure
Pr	Prandtl number
Ra	Rayleigh number
S	dimensionless concentration
Sc	Schmidt number
Sh	overall Sherwood number
T	dimensionless temperature
U, V	dimensionless velocity components in X, Y
X, Y	dimensionless Cartesian coordinates

Greek symbols

α	thermal diffusivity
β	volumetric expansion coefficient
Δ	difference value
v	kinematic viscosity of fluid
ρ	density
τ	dimensionless time
Ψ	dimensionless stream function
Θ	dimensionless heat function
Ω	dimensionless mass function

Subscripts

h	higher value
l	lower value
max, min	maximum, minimum
s	solutal
t	thermal

Superscript

*	dimensional variable

in salt-gradient solar ponds [23], or crystal growth control [24] and in heat and moisture transport in building elements [25–29], also warrant the investigation of double-diffusive convection induced by discrete heat and mass sources. To the best knowledge of the authors, no attention has been paid to the double-diffusive natural convection in closed porous enclosures with discrete heat and mass sources, though it has been received considerable studies in single-component natural convection [30–38]. It should be mentioned that Bergman and Ungan [24] have numerically and experimentally reported the transient evolution of convective flow induced by bottom heating with a heated strip placed beneath a salt-stratified layer with a top free surface, imposing the destabilizing temperature and stabilizing salinity gradients. Chen et al. [25] have numerically studied the steady mixed double-diffusive convection in a slot-ventilated enclosure subject to localized heating and salting. Zhao et al. [26–28] have investigated the double-diffusive natural convection induced by discrete thermosolutal sources in a porous/fluid enclosure. Liu et al. [29] have studied the thermosolutal convection driven by conditions of uniform heat and mass fluxes imposed along the portion of the two vertical walls.

The present work describes numerical results of steady-state double-diffusive natural convection induced by bottom heating and polluting with two finite thermal and pollutant strips symmetrically placed beneath a porous layer saturated with moist air. This situation can be found in many fields, such as grain storage, migration of moisture contained in fibrous insulation, floor heating and humidifying [7,8,13,15,16,26–29]. The porous medium considered here is modeled according to the Darcy–Brinkman formulation, which accounts for friction due to macroscopic shear and is more appropriated to describe the fluid flow in the porous matrix [15,16,27]. The effects of buoyancy ratio, thermal Rayleigh number, pitches of heat and pollutant sources and the permeability of the porous medium on the multiple steady convective solutions will also be illustrated and analyzed in this paper. Additionally, the fluid, heat and mass transport structures are presented by streamlines, heatlines and masslines, respectively, which are useful in investigating the convective heat and mass transfer [3,9,11–14,19,25–29,39].

2. Problem formulation

2.1. Physical model and assumptions

The physical domain under investigation is a two-dimensional fluid-saturated Darcy–Brinkman porous enclosure (see Fig. 1). The rectangular enclosure is of width L and height H (aspect ratio $Ar = L/H$), and the Cartesian coordinates (x, y), with the corresponding velocity components (u, v), are indicated herein. It is assumed that the third dimension of the enclosure is large enough so that the fluid, heat and mass transports are two-dimensional. Gravity acts in the negative y-direction. The discrete heat and pollutant sources are separately located on the left-half and right-half bottom, being of length L_t and L_s, respectively. The pitch between the right edge of the heat strip and the left edge of the mass strip is L_{ts}. They are located symmetrically with central line ($x = 0$) of the horizontal enclosure.

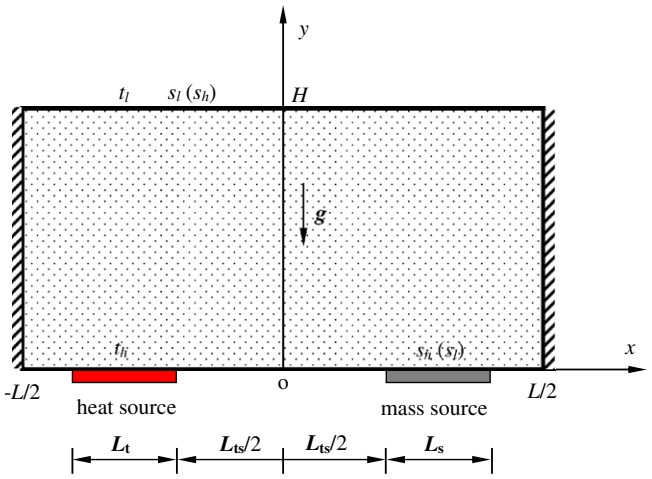

Fig. 1. Geometry and boundary conditions for the studied porous enclosure with discrete heat and contaminant sources.

The horizontal top wall of the enclosure is maintained at lower temperature t_l. Vertical walls and the bottom side excluding the discrete strips are assumed to be impermeable and perfect thermal insulations. Initially, the stationary fluid mixture and the confining walls are assumed to be at uniform temperature t_l and the same uniform concentration s_l. At $\tau^* = 0$, the temperature at the surface of the heated strip is suddenly raised to a higher-level t_h and maintained at this level thereafter. Meanwhile, the concentration of the fluid at the surface of the pollutant strip or at the top wall, depending on the stabilizing or destabilizing solutal buoyancy forces, is hypothesized to be abruptly elevated to a higher value s_h. Accordingly, vertical temperature and concentration gradients are imposed on the fluid, and the flow is then initiated and evolves under the action of the combined driving forces due to these gradients.

The fluid saturating the porous medium is a perfect two-component mixture, and this mixture is taken as a Newtonian–Fourier–Fick fluid. The porous matrix is assumed to be uniform and in local thermal and compositional equilibrium with the saturating fluid. Thermophysical properties are supposed constant. The flow is assumed to be laminar and incompressible. Viscous dissipation and porous medium inertia are not considered, and the Soret and Dufour effects are neglected. Density of the saturated fluid mixture is assumed to be uniform over all the enclosure, exception made to the buoyancy term, in which it is taken as a function of both the temperature t and concentration s through the Boussinesq approximation,

$$\rho = \rho_l[1 - \beta_t(t - t_l) - \beta_s(s - s_l)] \tag{1}$$

where ρ_l is the fluid density at temperature t_l and concentration s_l, and β_t and β_s are the thermal and concentration expansion coefficients, respectively. The above simplification is appropriate when both the components in the mixture have comparable molecular weights or when the mixture is dilute. In this study, for moist air at room conditions, β_t can assume the value near 0.0034 K^{-1} and β_s can assume values between 0.61 kg/kg (for pure dry air) and 0.38 kg/kg (for pure water vapor) [3,14].

It remains to be noted that, in the present work, the thermal levels are small and similar enough so that thermal radiation heat transfer between the walls is negligible, and the fluid is assumed to be radiatively non-participating [13,14]. Additionally, there are problems not considered related with transition to turbulence, and the condensation phenomenon when the medium that fills the enclosure is a gaseous mixture with a condensable component.

2.2. Model equations

By employing the aforementioned assumptions into the macroscopic conservation equations of mass, momentum, energy and species, a set of dimensionless governing equations is expressed as follows:

$$\frac{\partial U}{\partial X} + \frac{\partial V}{\partial Y} = 0 \tag{2}$$

$$\frac{\partial U}{\partial \tau} + \frac{\partial UU}{\partial X} + \frac{\partial VU}{\partial Y} = -\frac{\partial P}{\partial X} + \sqrt{\frac{Pr}{Ra_t}}\left(\frac{\partial^2 U}{\partial X^2} + \frac{\partial^2 U}{\partial Y^2}\right) - \sqrt{\frac{Pr}{Ra_t}}\frac{U}{Da} \tag{3}$$

$$\frac{\partial V}{\partial \tau} + \frac{\partial UV}{\partial X} + \frac{\partial VV}{\partial Y} = -\frac{\partial P}{\partial Y} + \sqrt{\frac{Pr}{Ra_t}}\left(\frac{\partial^2 V}{\partial X^2} + \frac{\partial^2 V}{\partial Y^2}\right) - \sqrt{\frac{Pr}{Ra_t}}\frac{V}{Da} + (T + NS) \tag{4}$$

$$\frac{\partial T}{\partial \tau} + \frac{\partial UT}{\partial X} + \frac{\partial VT}{\partial Y} = \frac{1}{\sqrt{Ra_t Pr}}\left(\frac{\partial^2 T}{\partial X^2} + \frac{\partial^2 T}{\partial Y^2}\right) \tag{5}$$

$$\frac{\partial S}{\partial \tau} + \frac{\partial US}{\partial X} + \frac{\partial VS}{\partial Y} = \frac{1}{Le\sqrt{Ra_t Pr}}\left(\frac{\partial^2 S}{\partial X^2} + \frac{\partial^2 S}{\partial Y^2}\right) \tag{6}$$

Non-dimensionalization of the governing equations has been achieved by defining the following dimensionless variables:

$$(X, Y) = (x, y)/H, \quad (U, V) = (u, v)/U_0, \quad \tau = \tau^* U_0/H \tag{7a}$$

$$P = (p + \rho_l g y)/[\rho_l U_0^2], \quad T = (t - t_l)/\Delta t, \quad S = (s - s_l)/\Delta s \tag{7b}$$

where H, $U_0 = (g\beta_t \Delta t H)^{1/2}$, H/U_0, $\Delta t = (t_h - t_l)$ and $\Delta s = (s_h - s_l)$ are used as characteristic scales for length, velocity, time, temperature and concentration, respectively. These scales can maintain balance of convection and diffusion terms [40,41]. Foregoing equations introduce the dimensionless parameters,

$$Pr = \nu/\alpha, \quad Da = K/H^2, \quad Ra_t = g\beta_t \Delta t H^3/\nu\alpha, \quad Le = \alpha/D, \quad N = \beta_s \Delta s/\beta_t \Delta t \tag{8}$$

where ν is the kinematics viscosity of the fluid, α and D, respectively are the thermal and molecular diffusivities of the combined fluid plus solid porous matrix medium, K is

the permeability of the porous medium, and g is the acceleration due to gravity. Since the particle Reynolds number is considered being less than unity in this work, the Forchheimer inertia term has been dropped from the momentum Eqs. (3) and (4) compared with the Darcy and Brinkman terms. The porosity of the porous layer, the ratios between effective viscosity and fluid viscosity, and the ratios of the thermophysical properties of the porous medium and of the fluid, have been implicitly set to unity [15,16,27,30]. Schmidt number can also be introduced as, $Sc = \nu/D = PrLe$.

2.3. Boundary conditions

Non-slip boundary conditions are imposed over the walls of the enclosure,

$$U = V = 0 \tag{9}$$

With such boundary conditions, it is assumed that the pollutant mass flow through the vertical walls is small enough in order to validate the use of zero normal velocity values at such walls. At the impermeable and perfect thermal insulated vertical walls,

$$\frac{\partial T}{\partial X} = \frac{\partial S}{\partial X} = 0, \quad X = -Ar/2 \quad \text{and} \quad X = +Ar/2, \quad 0 < Y < 1 \tag{10}$$

The same conditions are imposed on the bottom except the surface of the heat and contaminant sources, where the following boundary conditions are imposed:

$$T = 1 \ \text{and} \ \frac{\partial S}{\partial Y} = 0, \quad -(2L_t + L_{ts})/2H \leqslant X \leqslant -L_{ts}/2H, \quad Y = 0 \tag{11}$$

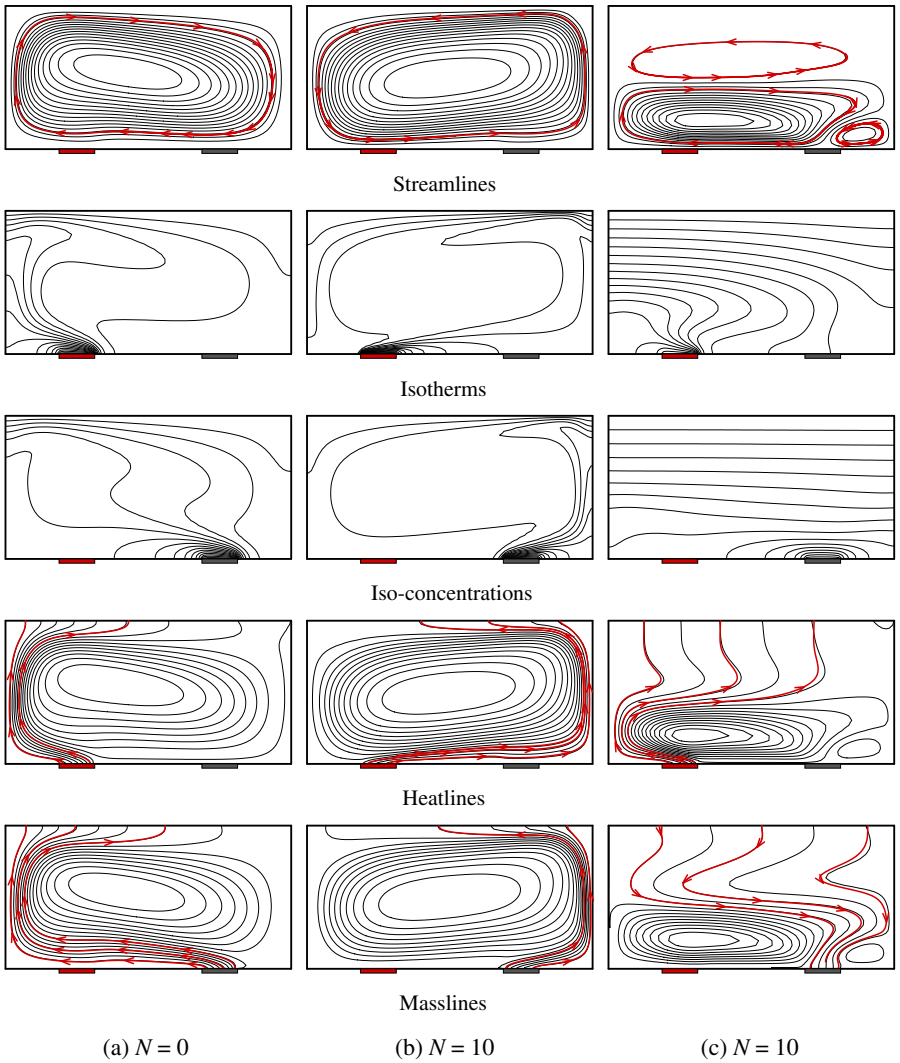

Fig. 2. Contour lines of stream function (top), temperature (top-1), concentration (top-2), heat function (top-3) and mass function (bottom) for $Ra_t = 10^5$, $Da = 10^2$ and $L_{ts} = 0.75H$. (a) $N = 0$ with upward mass transfer, $Nu = 2.575$, $Sh = 2.452$, $\Psi_{max} = 0.000$, $\Psi_{min} = -0.071$, $\Theta_{max} = 0.001$, $\Theta_{min} = -4.935$, $\Omega_{max} = 0.001$, and $\Omega_{min} = -4.558$; (b) $N = 10$ with destabilizing solutal buoyancy effect, $Nu = 4.878$, $Sh = 3.680$, $\Psi_{max} = 0.227$, $\Psi_{min} = -0.002$, $\Theta_{max} = 11.756$, $\Theta_{min} = -4.875$, $\Omega_{max} = 6.044$, and $\Omega_{min} = -3.679$; (c) N = 10 with stabilizing solutal buoyancy effect, $Nu = 1.563$, $Sh = -1.256$, $\Psi_{max} = 0.005$, $\Psi_{min} = -0.020$, $\Theta_{max} = 0.001$, $\Theta_{min} = -3.973$, $\Omega_{max} = 1.589$, and $\Omega_{min} = -2.038$.

$$S = 1 \text{ and } \frac{\partial T}{\partial Y} = 0, \quad L_{ts}/2H \leqslant X \leqslant (2L_s + L_{ts})/2H, \quad Y = 0 \text{ (upward mass transfer)} \tag{12a}$$

$$S = 0 \text{ and } \frac{\partial T}{\partial Y} = 0, \quad L_{ts}/2H \leqslant X \leqslant (2L_s + L_{ts})/2H, \quad Y = 0 \text{ (downward mass transfer)} \tag{12b}$$

Over the top wall,

$$T = 0, \quad S = 0, \quad -Ar/2 \leqslant X \leqslant +Ar/2, \quad Y = 1 \text{ (upward mass transfer)} \tag{13a}$$

$$T = 0, \quad S = 1, \quad -Ar/2 \leqslant X \leqslant +Ar/2, \quad Y = 1 \text{ (downward mass transfer)} \tag{13b}$$

The foregoing prescription of T and S over the horizontal walls (Eqs. (11), (12a) and (13a)) can lead to a situation of destabilizing thermal and solutal buoyancy effects. However, the boundary conditions (Eqs. (11), (12b) and (13b)) lead to a situation of opposing heat and moisture gradients, which weakens the net buoyancy.

2.4. Convective transport and visualization

For each time step the dimensionless heat and mass transports for a given horizontal line ($Y = Y_0$) of the network are determined by means of the expression [19],

$$Nu = \int_{-\frac{Ar}{2}}^{+\frac{Ar}{2}} \left(\sqrt{Ra_t Pr}\, VT - \frac{\partial T}{\partial Y} \right) \mathrm{d}X,$$

$$Sh = \int_{-\frac{Ar}{2}}^{+\frac{Ar}{2}} \left(Le\sqrt{Ra_t Pr}\, VS - \frac{\partial S}{\partial Y} \right) \mathrm{d}X \tag{14}$$

The global Nusselt and Sherwood numbers are obtained by taking the average of all the lines. The calculations

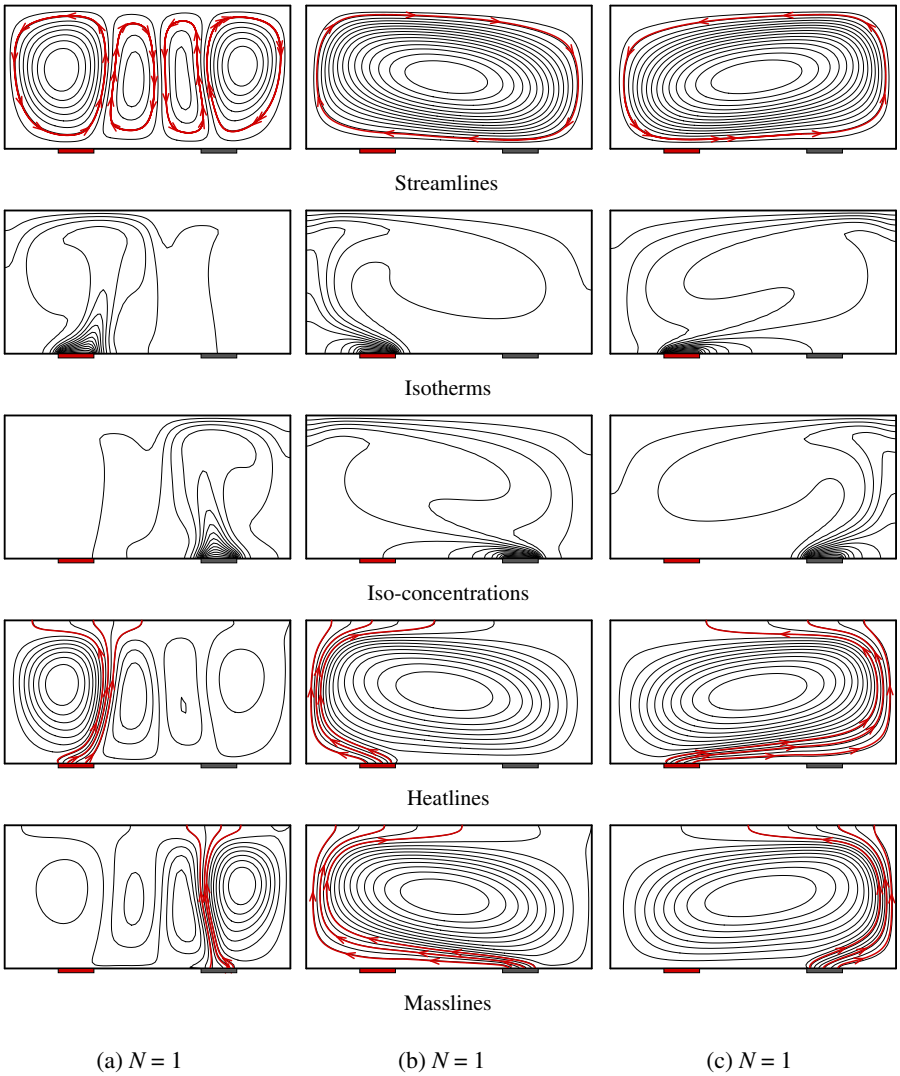

Fig. 3. Contour lines of stream function (top), temperature (top-1), concentration (top-2), heat function (top-3) and mass function (bottom) for $Ra_t = 10^5$, $Da = 10^2$, $L_{ts} = 0.75H$, and with destabilizing solutal buoyancy effect. (a) $Nu = 2.458$, $Sh = 2.260$, $\Psi_{max} = 0.068$, $\Psi_{min} = -0.060$, $\Theta_{max} = 3.366$, $\Theta_{min} = -3.641$, $\Omega_{max} = 1.058$, and $\Omega_{min} = -4.654$; (b) $Nu = 2.618$, $Sh = 3.203$, $\Psi_{max} = 0.000$, $\Psi_{min} = -0.124$, $\Theta_{max} = 0.001$, $\Theta_{min} = -6.264$, $\Omega_{max} = 0.002$, and $\Omega_{min} = -8.138$; (c) $Nu = 3.440$, $Sh = 2.502$, $\Psi_{max} = 0.120$, $\Psi_{min} = 0.000$, $\Theta_{max} = 6.253$, $\Theta_{min} = -3.441$, $\Omega_{max} = 2.869$, and $\Omega_{min} = -2.502$.

are continued until a result independent of time was obtained.

In order to clearly exhibit the fluid, heat and contaminant transport characteristics of double-diffusive natural convection, a recently developed visualization technique of convective transport paths is employed [3,9,11–14,19,25–29,39]. In terms of above continuity, energy, and concentration conservation equations, the dimensionless stream function Ψ, heat function Θ, and mass function Ω are defined respectively as follows [19]:

Stream function

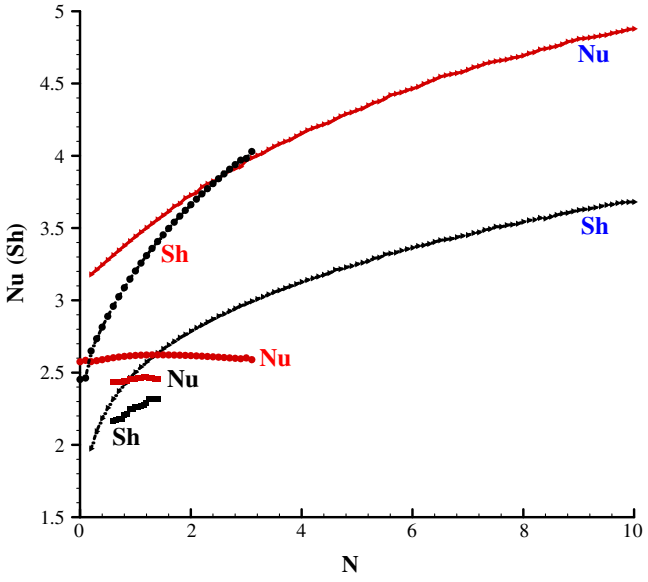

(a) Destabilizing solutal buoyancy effect

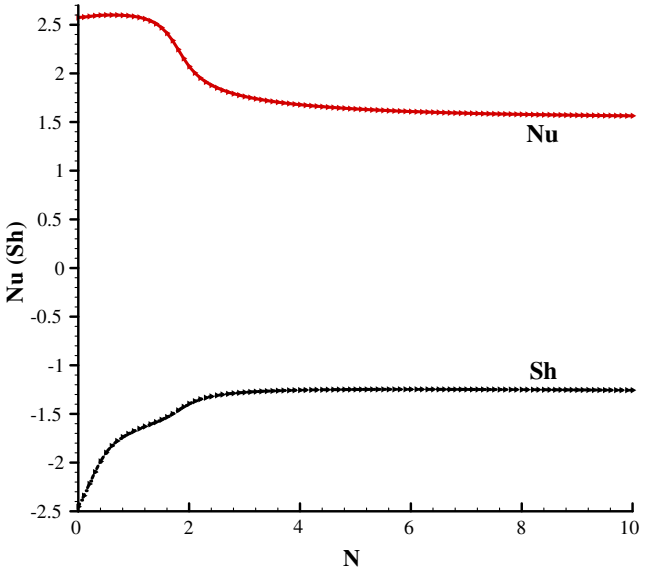

(b) Stabilizing solutal buoyancy effect

Fig. 4. The effect of buoyancy ratio on the overall Nusselt (Nu) and Sherwood (Sh) numbers for $Ra_t = 10^5$, $Da = 10^2$ and $L_{ts} = 0.75H$, with boundary conditions of destabilizing solutal flow (a) and those of stabilizing solutal flow (b).

$$\frac{\partial \Psi}{\partial Y} = U, \quad -\frac{\partial \Psi}{\partial X} = V \tag{15}$$

Heat function

$$\frac{\partial \Theta}{\partial Y} = \sqrt{Ra_t Pr}UT - \frac{\partial T}{\partial X}, \quad -\frac{\partial \Theta}{\partial X} = \sqrt{Ra_t Pr}VT - \frac{\partial T}{\partial Y} \tag{16}$$

Mass function

$$\frac{\partial \Omega}{\partial Y} = Le\sqrt{Ra_t Pr}US - \frac{\partial S}{\partial X}, \quad -\frac{\partial \Omega}{\partial X} = Le\sqrt{Ra_t Pr}VS - \frac{\partial S}{\partial Y} \tag{17}$$

where the following relations are made for dimensionalization:

$$\Psi = \frac{\Psi^*}{\rho\alpha}, \quad \Theta = \frac{\Theta^*}{k\Delta t}, \quad \Omega = \frac{\Omega^*}{\rho D \Delta s} \tag{18}$$

The corresponding contour lines, streamlines, heatlines and masslines, are representative of the transport pathlines of fluid, heat and contaminant. Once known the flow, temperature and concentration fields, the stream function, heat function and mass function can be obtained using the integration method [19].

3. Numerical technique and validation

Finite volume method (FVM) is applied to discretize the governing equations on a staggered grid system [42]. In the course of discretization, the third-order deferred correction QUICK scheme [43] and a second order central difference scheme are respectively implemented for the convection and diffusion terms. The SIMPLE algorithm was chosen to numerically solve the governing differential equations in their primitive form [41,42]. To obtain better convergence properties, the unsteady terms in these equations were implicitly treated and hence approximated by backward differencing. For each time step, the discretized equations were solved by a line-by-line procedure, combining the tri-diagonal matrix algorithm (TDMA) and the successive over-relaxation (SOR) iteration.

Numerical experiments were performed to establish that the number and the distribution of the control-volumes are sufficient to resolve the thinnest boundary layer, with more control volumes concentrated near boundaries and sources. During the program tests, a systematic grid independence study was conducted, and then the final grid resolution of 81×41 was selected at the balance between the calculation accuracy and the speed for $Ar = 2$. The time interval, first set at a relatively small value from 10^{-4} to 10^{-3} depending on Ra_t and N, is successively enlarged.

The convergence criteria are based on maximum errors in global mass, energy and species imbalances. Convergence was insured when the maximum errors become less than 10^{-3}. The current numerical technique has been very successfully used and validated in a series of recent papers, including single-component natural convection [38–41], conjugate heat transfer [39–41], double-diffusive mixed

convection [25] and double-diffusive natural convection in fluid or porous enclosures [19,26–29].

4. Results and discussion

As was already noted above, the problem under investigation is governed by nine non-dimensional groups: the thermal Rayleigh number Ra_t, Prandtl number Pr, buoyancy ratio N, Lewis number Le, Darcy number Da, aspect ratio Ar, size of heat source L_t/H, size of contaminant source L_s/H, and the pitch between discrete sources L_{ts}/H. It is a formidable task to perform computations covering wide ranges of all these parameters. Instead, enclosure aspect ratio and sizes of both sources are maintained at $Ar = 2$ and $L_t/H = L_s/H = 0.25$, respectively. Simultaneously, results were obtained for a given binary gas mixture with Pr and Sc fixed at 0.7 and 0.6, respectively, thus giving $Le \approx 0.8$ [5,10,12–14,19]. Attention is therefore focused herein on the effects of the buoyancy ratio N, thermal Rayleigh number Ra_t, strip pitch L_{ts}/H, and Darcy number Da. The Brinkman extended Darcy model has been used through the study: in the first study, the Da is fixed at 10^2 (approaching to the limiting case of pure viscous fluid), then the influence due to Brinkman term due to increasing viscous forces ($Da = 10^{-6}$–10^3) is analyzed.

The stream function will be used to identify the sense and magnitude of the fluid circulation. The coordinates are chosen such that counter-clockwise (or clockwise) movement will be associated with positive (or negative) Ψ. Similar relations are set for heat flow and heat function Θ, and for solute flow and mass function Ω. The computed streamlines, isotherms, iso-concentrations, heatlines and masslines are plotted in the following figures. The intervals of these isopleths are $\Delta\varphi = (\varphi_{max} - \varphi_{min})/16$, where φ

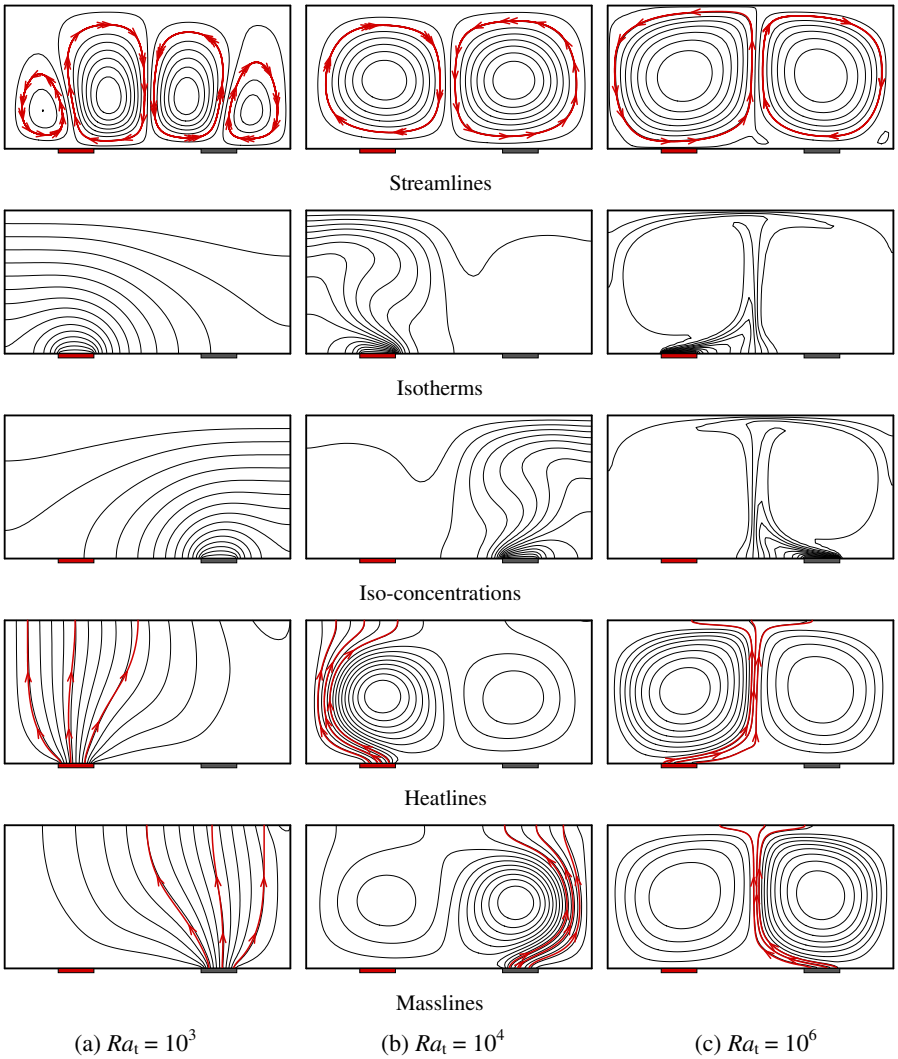

Fig. 5. Contour lines of stream function (top), temperature (top-1), concentration (top-2), heat function (top-3) and mass function (bottom) for $L_{ts} = 0.75H$, $Da = 10^2$, $N = 1$ with upward mass transfer. (a) $Ra_t = 10^3$, $Nu = 0.890$, $Sh = 0.889$, $\Psi_{max} = 0.003$, $\Psi_{min} = -0.003$, $\Theta_{max} = 0.000$, $\Theta_{min} = -0.890$, $\Omega_{max} = 0.000$, and $\Omega_{min} = -0.889$; (b) $Ra_t = 10^4$, $Nu = 1.776$, $Sh = 1.673$, $\Psi_{max} = 0.091$, $\Psi_{min} = -0.085$, $\Theta_{max} = 0.000$, $\Theta_{min} = -3.111$, $\Omega_{max} = 1.182$, and $\Omega_{min} = -1.674$; (c) $Ra_t = 10^6$, $Nu = 5.484$, $Sh = 4.979$, $\Psi_{max} = 0.104$, $\Psi_{min} = -0.103$, $\Theta_{max} = 16.716$, $\Theta_{min} = -14.552$, $\Omega_{max} = 6.796$, and $\Omega_{min} = -18.144$.

stands for Ψ, T, S, Θ or Ω. Discrete sources on the floor are indicated by heavy lines.

4.1. Effect of buoyancy ratio

The thermal Rayleigh number, Darcy number and pitch of strips are maintained at $Ra_t = 10^5$, $Da = 10^2$ and $L_{ts} = 0.75H$, respectively. Typical flow charts will be presented when the temperature gradient is destabilizing and when the concentration gradient is either stabilizing or destabilizing.

For $N = 0$ with upward mass transfer, the flow is driven solely by the vertical destabilizing thermal gradient. Upon starting the numerical code with the rest state $\Psi = T = S = 0$ as initial conditions, a unicellular clockwise circulation develops in Fig. 2a. Isotherms and iso-concentrations show steeper gradients near the heating and polluting elements respectively, and the concentration filed that rides on the heat-transfer-driven flow as depicted in Fig. 2 depends to a significant degree on the Lewis number. With the Lewis number less than unity, the mass transfer process is diffusion dominated. The thermal boundary layer is expected to be thinner than the hydrodynamic boundary layer, and the hydrodynamic boundary layer is either comparable to or thinner than the solutal boundary layer. The net result is that the temperature field in the core of the cavity tends to be uniform, while the concentration is linearly stratified in the right-half zone. However, the masslines take the similar pattern of the heatlines due to the comparative thermal and solutal diffusivities.

When N increases to 10, the flow is driven mainly by the destabilizing vertical compositional gradient. As observed in Fig. 2b, both thermal and solutal buoyancy effects are augmenting each other and thus they simultaneously accel-

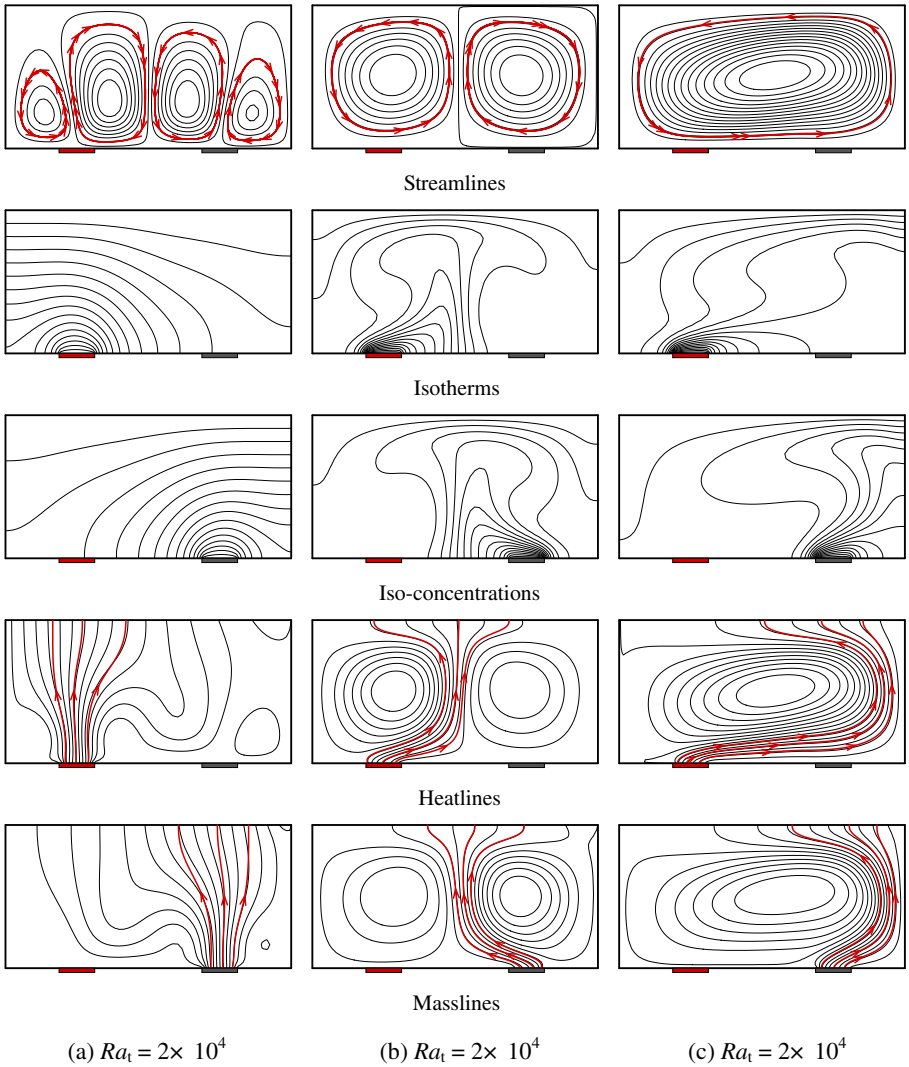

Fig. 6. Contour lines of stream function (top), temperature (top-1), concentration (top-2), heat function (top-3) and mass function (bottom) for $L_{ts} = 0.75H$, $Da = 10^2$ and $N = 1$ with upward mass transfer. (a) $Nu = 0.915$, $Sh = 0.904$, $\Psi_{max} = 0.004$, $\Psi_{min} = -0.004$, $\Theta_{max} = 0.028$, $\Theta_{min} = -0.890$, $\Omega_{max} = 0.010$, and $\Omega_{min} = -0.889$; (b) $Nu = 2.120$, $Sh = 1.954$, $\Psi_{max} = 0.097$, $\Psi_{min} = -0.097$, $\Theta_{max} = 2.041$, $\Theta_{min} = -3.168$, $\Omega_{max} = 0.836$, and $\Omega_{min} = -3.474$; (c) $Nu = 2.262$, $Sh = 1.921$, $\Psi_{max} = 0.117$, $\Psi_{min} = 0.000$, $\Theta_{max} = 2.259$, $\Theta_{min} = -2.263$, $\Omega_{max} = 1.166$, and $\Omega_{min} = -1.921$.

erate the flow counter-clockwise. The intensity of the eddy flow, measured by the absolute of the extreme value of Ψ, has been enhanced three times higher than that of heat-driven flow limit. Temperature and concentration fields in the core region are observed to be uniform. The isotherms and iso-concentration lines indicate that both the thermal and concentration fields have boundary layer character, their thickness approximately equal to that of the hydrodynamic boundary layer. Heatlines and masslines have the similar pattern of counter-clockwise heat or mass flows.

Whereas, as the boundary conditions of downward mass transfer (Eqs. (12b) and (13b)) are imposed and buoyancy ratio N is approaching value of infinite, a strong stabilizing vertical solutal gradient prevails within the gaseous layer for which the fluid within the layer is expected to remain at rest. As N equaling 10, illustrated in Fig. 2c, there is a competition between thermal and solutal buoyancy forces. The rotational motion, indicated by the streamlines, is induced by the corresponding non-uniform destabilizing temperature distributions. The flow pattern is observed to be multi-cellular with a large clockwise rotating cell and two counter-clockwise rotating cells, one beginning at the right boundary separating the pollutant strip and impermeable section of the bottom surface, the other occurring in the overlying the solute-stratified fluid and induced by shear stresses due to convection in the main cell. The isotherms are skewed towards the heating element and show unstable stratification in the upper region, while the iso-concentrations show stable stratification in the entire region. Stabilizing density gradients develop at the interface separating the convecting fluid from the solute-stratified fluid and inhibit further upward propagation of convective conditions. As a consequence, heat conduction and solutal diffusion are dominant in the upper region, which can be demonstrated by the heatlines and masslines parallel penetrating from fluid to the top sink.

Aforementioned flow charts are all obtained using the rest state, $\Psi = T = S = 0$ as initial conditions. However, multiple steady solutions are possible when different initial conditions are used. For a classical Bénard situation [5,6,33], the resulting cell(s) can rotate indifferently clockwise or counter-clockwise, giving rise to two different convection states. Thus, using rest state as initial values for Bénard convection, the direction of rotation of the cell is not imposed by the physics of the problem but is induced by the round-off errors generated in the numerical computations. In contrast, when the porous enclosure is partially heated and contaminated by the bottom, the existence of several cells and the direction of their rotation seem to be imposed a priori, the fluid being ascendant above the thermal and solutal elements with positive volumetric expansion coefficients. An example of this flow configuration is given in Fig. 3a with $N = 1$. These flows, which develop from rest as initial conditions, can be referred to 'natural' flow. The flow field in this horizontal enclosure with upward transfer consists of a series of roll cells, each counter-rotating in the opposite direction to its neighbors. Thermal convection with two counter-rotating cells in the left-half region is expected to initiate at the right edge of the heated section, while solutal convection including with the other two cells in the right-half region initiate at the left edge of the pollutant segment. However, it is also possible to obtain a convective pattern such that the fluid motion above the thermal or solutal element is not ascendant but rather moves down toward it. Such reversed circulations, called 'anti-natural' solute and heat flows, are illustrated in Fig. 3b and c, respectively. Correspondingly, solute (heat) takes more paths to reach the sink, as illuminated by the masslines and heatlines in Fig. 3b and c, respectively. Close scrutiny of temperature fields in Fig. 3a–c shows that, the ascending streams are hotter than descending ones, providing the driving force in the respective directions of motion. Similar observations can be found in concentration fields.

The effect of buoyancy ratio N on the overall Nusselt and Sherwood numbers is depicted in Fig. 4 with upward mass transfer and downward mass transfer, respectively. In general, heat and mass transfer rates of destabilizing solutal gradients ($N \gg 0$ in Fig. 4a) are greater than that of stabilizing solutal gradients ($N \gg 0$ in Fig. 4b). For the latter case, shown in Fig. 4b, the overall Nusselt number and Sherwood number approach 1.5 and -1.2, respectively, which belongs to the solutal-dominated opposing flow, giving rise to a weak multi-cellular flow as illustrated in Fig. 2c. Gradually decreasing N from 10 to lower values, the top cell shown in Fig. 2c would vanish ($N = 2.2$), and the flow intensity increases accordingly. As illustrated in Fig. 4b, the heat and mass transfer rates also increase with the decreasing N.

In terms of destabilizing thermal and solutal buoyancy effects (Fig. 4a), it can be observed that the Sherwood number unexpectedly exceeds the value of the Nusselt number

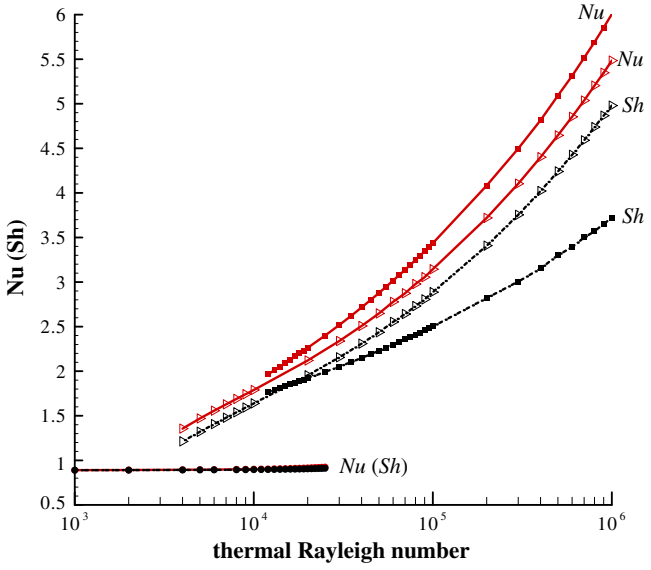

Fig. 7. The effect of thermal Rayleigh number Ra_t on the overall Nusselt and Sherwood numbers for $N = 1$, $Da = 10^2$ and $L_{ts} = 0.75H$.

greatly as the buoyancy ratio is continuing increased from zero. Masslines pattern in Fig. 3b shows that the low-concentration fluid sweeps along the bottom pollutant segment and it continues to be soluted for a longer distance, thus enhancing the mass transfer potential. The thermal-dominated flow, exemplified by the flow pattern of Fig. 3b, could be sustained for $0.0 \leqslant N \leqslant 3.1$. On the other hand, when decreasing N from 10, the solutal-dominated aiding flow identified in Fig. 2b can be maintained to $N = 0.2$. The overall heat transfer rate is observed to remain higher than the mass transfer rate. Observing from Figs. 2b and 3c, heatlines pattern illuminates that the cold fluid sweeps the heated strip longer, and greatly increasing the heat transfer potential. In addition to the aforementioned two different solutions, a third possible solution, similar to that illustrated in Fig. 3a can be maintained in the range of $0.6 \leqslant N \leqslant 1.4$ as presented in Fig. 4a. Heatlines and masslines in Fig. 3a illuminate that the 'natural' heat and solute flows greatly shorten the heat and mass transfer interfaces, thus decreasing heat and mass transfer rates together.

4.2. Effect of thermal Rayleigh number

Fig. 5 presents steady-state contour maps for various values of Ra_t for $L_{ts} = 0.75H$, $N = 1$ and $Da = 10^2$. The condition $N = 1$ here means that the flow is dominated by equal but destabilizing effects of both thermal and compositional buoyancies.

As shown in Fig. 5a, Ra_t is low (10^3), two pairs of counter-rotating cells develop near both symmetry planes of the discrete sources, one is induced by thermal buoyancy, the other by solutal force. The isotherms and iso-concentrations uniformly and annularly cluster around the heat source and the pollutant source, respectively. Heat and sol-

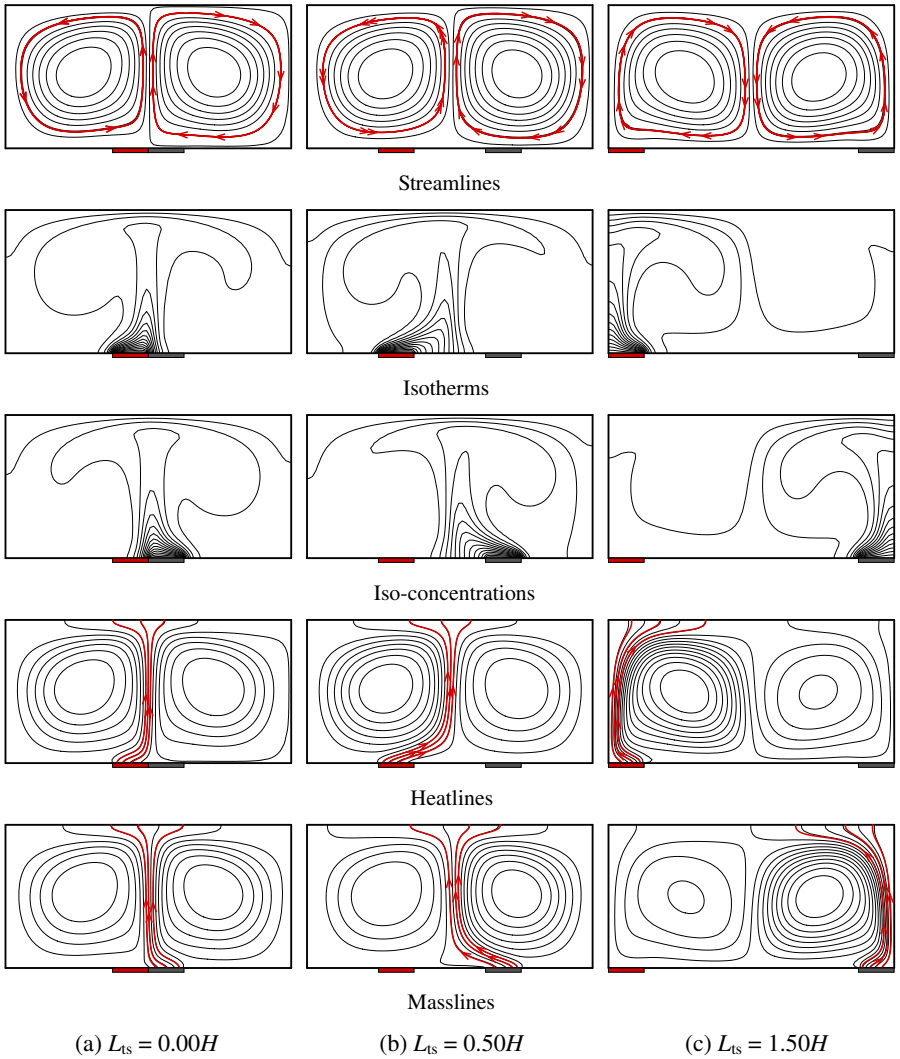

Fig. 8. Contour lines of stream function (top), temperature (top-1), concentration (top-2), heat function (top-3) and mass function (bottom) for $Ra_t = 10^5$, $Da = 10^2$ and $N = 1$ with upward mass transfer. (a) $L_{ts} = 0$, $Nu = 2.664$, $Sh = 2.491$, $\Psi_{max} = 0.089$, $\Psi_{min} = -0.090$, $\Theta_{max} = 2.738$, $\Theta_{min} = -5.131$, $\Omega_{max} = 1.871$, and $\Omega_{min} = -4.660$; (b) $L_{ts} = 0.5H$,$Nu = 2.990$, $Sh = 2.754$, $\Psi_{max} = 0.098$, $\Psi_{min} = -0.101$, $\Theta_{max} = 4.142$, $\Theta_{min} = -5.746$, $\Omega_{max} = 2.000$, and $\Omega_{min} = -6.143$; (c) $L_{ts} = 1.5H$, $Nu = 2.012$, $Sh = 1.874$, $\Psi_{max} = 0.076$, $\Psi_{min} = -0.067$, $\Theta_{max} = 0.000$, $\Theta_{min} = -4.511$, $\Omega_{max} = 2.234$, and $\Omega_{min} = -1.876$.

ute are also transported from source to sink paralleling to the vertical wall. As Ra_t is increased to 10^4, streamlines consist of only two cells (Fig. 5b), which are counter-rotating and subject to destabilizing thermal and solutal forces, respectively. From the values of Ψ_{max} and Ψ_{min} it is observed that the convection strength of this bi-cellular convection is much higher than that of quad-cellular flow pattern. Due to the strength of convection, the existence of a temperature (concentration) gradient reversal is observed to occur in the core of the left (right) half region. Heatlines and masslines illuminate that heat and solute are still transported in the shortcut path. As Ra_t equaling 10^5, shown in Fig. 3a, the streamlines consist of four counter-rotating cells again. The two cells immediately adjacent to the walls are larger than those in the middle. The intensity of the flow in Fig. 3a is decreased when comparing with that of $Ra_t = 10^4$, it is however about 20 times stronger than that of $Ra_t = 10^3$ judging from the maximum values of the respective stream functions. The temperature (concentration) field is distorted and stratified most at the locations where the thermal-driven (solutal-driven) convection was moving up or down. The effect of increasing thermal Rayleigh number is to produce a plume-like flow above the heated and contaminated region and an adverse stratification in the respective core. When Ra_t is increased to 10^6, as illustrated in Fig. 5c, the temperature (concentration) field in the left (right) half core is noticed to be almost uniform. Again, the flow consists of two cells, with the enhanced strength of the flow eddy and the reversal rotations. As a result, the hot and high-concentration fluid effectively dips the top sink, and the heat and mass transfer rates are enhanced greatly.

Apart from the foregoing natural solutions (using rest state as initial conditions), other flow states can be

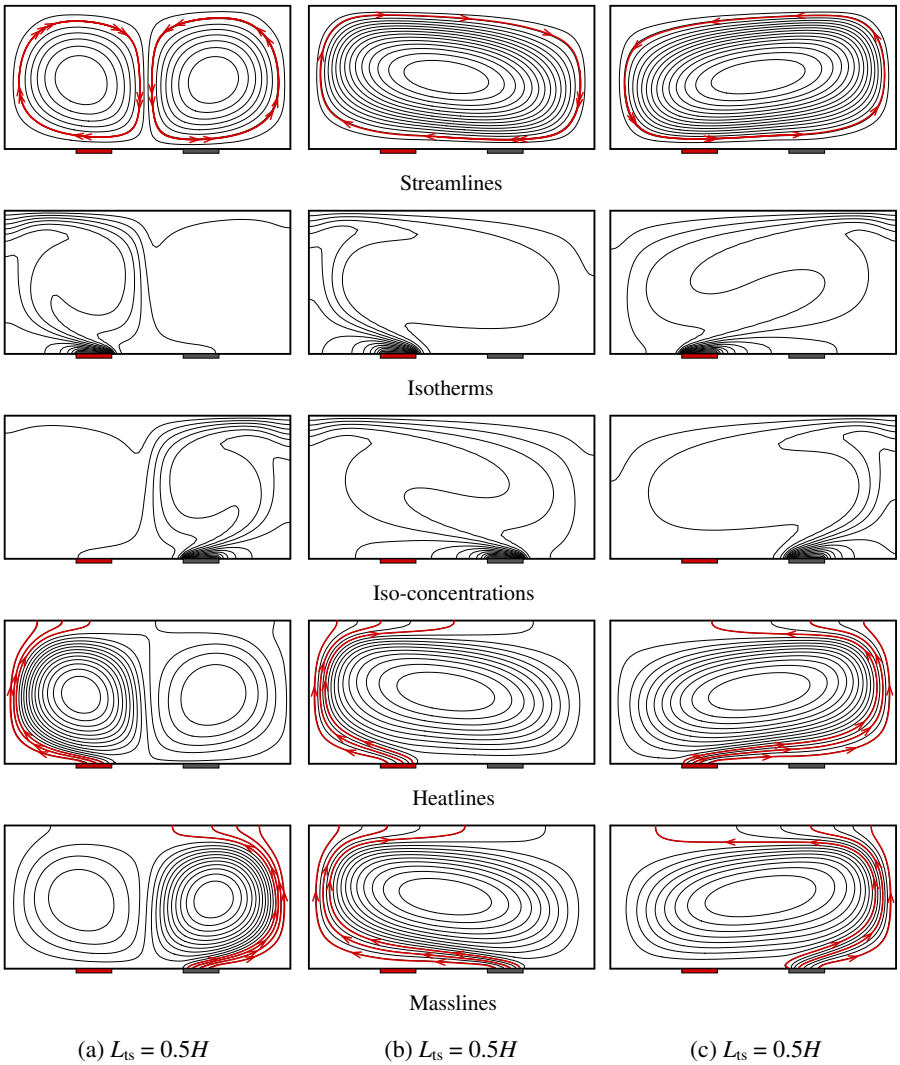

Fig. 9. Contour lines of stream function (top), temperature (top-1), concentration (top-2), heat function (top-3) and mass function (bottom) for $L_{ts} = 0.50H$, $Ra_t = 10^5$, $Da = 10^2$, and $N = 1$ with upward mass transfer, and (a) $Nu = 3.251$, $Sh = 3.070$, $\Psi_{max} = 0.111$, $\Psi_{min} = -0.102$, $\Theta_{max} = 0.009$, $\Theta_{min} = -10.212$, $\Omega_{max} = 6.001$, and $\Omega_{min} = -3.082$; (b) $Nu = 2.815$, $Sh = 3.255$, $\Psi_{max} = 0.000$, $\Psi_{min} = -0.128$, $\Theta_{max} = 0.004$, $\Theta_{min} = -7.149$, $\Omega_{max} = 0.005$, and $\Omega_{min} = -8.338$; (c) $Nu = 3.468$, $Sh = 2.660$, $\Psi_{max} = 0.122$, $\Psi_{min} = 0.000$, $\Theta_{max} = 6.186$, $\Theta_{min} = -3.477$, $\Omega_{max} = 3.231$, and $\Omega_{min} = -2.665$.

obtained if different initial conditions were chosen. It is seen from Fig. 6a–c, three modes of convection are possible for given values of N, Da, L_{ts} and $Ra_t = 2 \times 10^4$. The first solution, Fig. 6a, obtained by using the flow configuration of Fig. 5a as initial conditions, is observed to be almost similar to that in Fig. 5a. For the second solution, Fig. 6b, a flow pattern akin to that of Fig. 5c, is obtained through gradually decreasing Ra_t from 10^6 to 2×10^4. The results indicate that the flow intensity of Fig. 6b remains strong and it is about 25 times higher than that of Fig. 6a. For the third solution, Fig. 6c, the rest state $\Psi = T = S = 0$ was used as initial conditions, the solutally driven unicellular core flow spans now completely the enclosure. For this situation, 'anti-natural' heat flow occurs and the heat transfer potential thus increases, however, the mass transfer is decreased when comparing with the second solution of Fig. 6b. Similar results can be found in Fig. 3c of $Ra_t = 10^5$.

The effects of thermal Rayleigh number on the overall Nusselt and Sherwood numbers are illustrated in Fig. 7 for $L_{ts} = 0.75H$, $N = 1$ and $Da = 10^2$. When Ra_t is small enough, the convective motion is weak such that the heat and solute transport in diffusion modes, similar to that of Figs. 5a and 6a. Upon increasing Ra_t from 10^3, it was found that this flow regime with the symmetric and multi-cellular flow structure depicted in Fig. 6a could be maintained up to approximately 2.5×10^4. On the contrary, upon decreasing Ra_t from 10^6, the flow regime of high intensity can be maintained till Ra_t is lower than 4.0×10^3. Furthermore, for $1.2 \times 10^4 \leqslant Ra_t \leqslant 10^6$, a unicellular flow exemplified by Fig. 6c can be maintained such that Nusselt and Sherwood numbers are enhanced and inhibited respectively comparing with the foregoing solutions.

4.3. Effect of the strip pitch

To demonstrate the effect of segment pitch L_{ts} on the heat and mass transport structures, thermal Rayleigh number, Darcy number and the buoyancy ratio are fixed at 10^5, 10^2 and 1.0, respectively. When the thermal and solutal segments contact each other ($L_{ts} = 0$), shown in Fig. 8a, the upward penetration of convective condition develops from the rest state. This condition allows formation of two convective rolls in the X-direction with alternating clockwise and counter-clockwise rotation. The heated fluid takes on the appearance of a mushroom-shaped thermal rising from the center of the heated strip. The rising fluid is subsequently cooled at the top sink and descends at left and right top corners, as evidenced by the streamlines and isotherms. Similar solute flow observations can be found from the isoconcentrations. As the thermal and solutal segments shift to left and right sides, respectively (i.e., L_{ts} increases monotonically), the shear forces established at the bicellular interface decreases and thus the flow intensity increases accordingly, which can be demonstrated from the comparison of Fig. 8a and b. However, if the L_{ts} kept increasing, multi-cellular flow emerges (as shown in Fig. 3a), and consequently the strength of the convective motions decreases; the fluid rotation reverse would occur. An example of the final reverse flow configuration is given in Fig. 8c for the case of the heated and soluted strips touching the left and right sides, respectively ($L_{ts} = 1.50H$).

Excluding the natural solution disclosed in Fig. 8, it is still possible to obtain other steady convective patterns. Fig. 9a–c illustrate exemplary three different possible solutions for $L_{ts} = 0.5H$. The following initial conditions have to be chosen carefully to obtain the multiple solutions. The first solution, Fig. 9a, obtained by using the flow configuration of Fig. 8c as initial condition, is observed to be almost similar to that in Fig. 8c. The convective strength, measured by the absolute of the extremum value of the stream function, is enhanced about 1.5 times higher than that in Fig. 8c. Its heat and mass transfer in Fig. 9a is even vigorous than that in Fig. 8b due to the fact that heat and solute flows centrally descend from the top to fully sweep the heat and mass sources, respectively. As the heat-transfer-driven flow and solute-dominated aiding flow illustrated in Fig. 2a and b are used as initial conditions, the second and the third solutions shown in Fig. 9b and c can be obtained respectively, where the thermal (solutal) buoyancy is still strong enough to induce a primary cell circulating clockwise (anti-clockwise) along the entire enclosure walls. The convection strength of the unicellular flow pattern is both slightly stronger than that of the bicellular flow in Fig. 9a, while the heat and mass transfer potentials are inhibited and enhanced respectively in Fig. 9b, and the heat and mass transfer potentials are

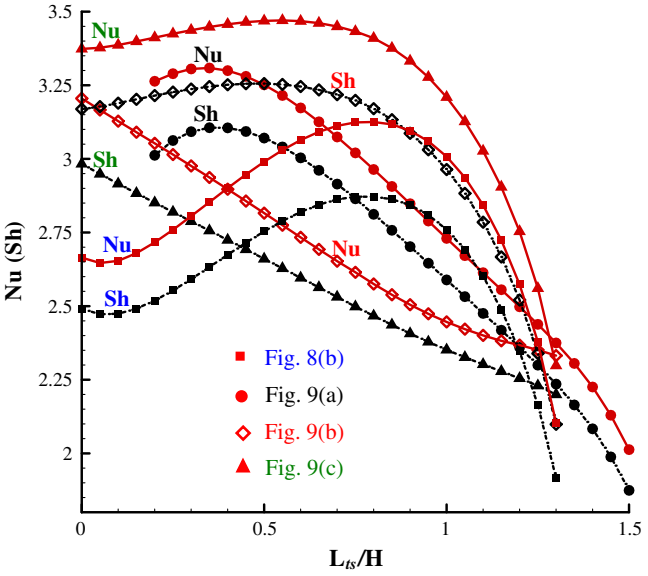

Fig. 10. Overall Nusselt and Sherwood numbers as functions of discrete source pitch L_{ts}/H for $Ra_t = 10^5$, $Da = 10^2$, and $N = 1$ with upward mass transfer. Filled square, filled circle, open diamond and filled delta symbol shapes represent the cases corresponding to Fig. 8b and Fig. 9a–c, respectively.

enhanced and inhibited respectively in Fig. 9c. Similar flow patterns and associated causes can be found in Fig. 3b and c.

The effect of strip pitch L_{ts}/H on the overall Nusselt and Sherwood numbers is depicted in Fig. 10 for $Ra_t = 10^5$, $Da = 10^2$ and $N = 1$ with upward mass transfer. For $L_{ts} = 0$, comparing these possible solutions, heat and mass transfer is minimum when using $\Psi = T = S = 0$ as initial values. When the segment pitch L_{ts} increases, the heat and mass transfer rates first reach a maximum value at $L_{ts} = 0.8H$ and then appreciably decrease as the L_{ts} approaches $1.3H$. However, for the case corresponding to Fig. 9a, the curve of heat and mass transfer almost increase monotonically with decreasing L_{ts} from $1.5H$ to $0.35H$, and then decrease slightly with L_{ts} decreasing to $0.2H$.

For the aforementioned two possible bicellular solutions indicated by filled square and circle symbols, the curves of Nusselt and Sherwood numbers almost parallel each other and the value of overall heat transfer rate is higher than that of mass transfer due to the Lewis number is lower than unity. However, for the unicellular flow case corresponding to Fig. 9b, overall mass transfer rates have been enhanced greatly such that it is 1.2 times higher than that of heat transfer at some strip pitches. On the contrary, for the flow pattern corresponding to Fig. 9c, the heat transfer potential is strengthened significantly such that it is the highest one comparing with other possible solutions; while the mass transfer rate decreases abruptly with increasing pitch L_{ts} such that it represents the lowest one for $0.45 < L_{ts}/H < 1.2$. Both unicellular flow cases corresponding to Fig. 9b and c can be sustained for $0 < L_{ts}/H < 1.3$, a smaller range of the governing parameter than the natural flow. Close scrutiny of the curves in Fig. 10 shows that, for $L_{ts}/H > 1.3$, no multiple states are possible.

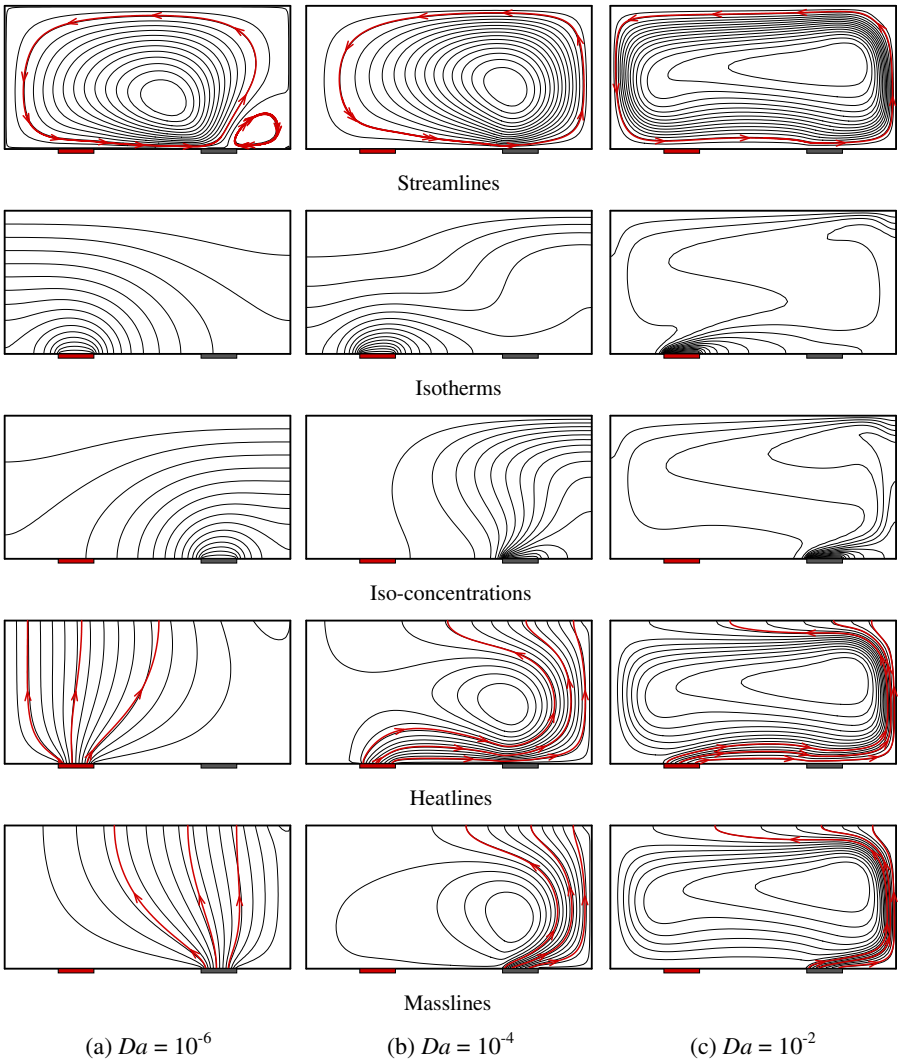

Fig. 11. Contour lines of stream function (top), temperature (top-1), concentration (top-2), heat function (top-3) and mass function (bottom) for $L_{ts} = 0.75H$, $Ra_t = 10^5$, and $N = 10$ with upward mass transfer. (a) $Nu = 0.889$, $Sh = 0.889$, $\Psi_{max} = 0.0001$, $\Psi_{min} = 0.000$, $\Theta_{max} = 0.000$, $\Theta_{min} = -0.889$, $\Omega_{max} = 0.000$,and $\Omega_{min} = -0.889$; (b) $Nu = 1.295$, $Sh = 2.012$, $\Psi_{max} = 0.020$, $\Psi_{min} = 0.000$, $\Theta_{max} = 0.402$, $\Theta_{min} = -1.295$, $\Omega_{max} = 0.683$, and $\Omega_{min} = -2.012$; (c) $Nu = 3.597$, $Sh = 3.695$, $\Psi_{max} = 0.114$, $\Psi_{min} = -0.002$, $\Theta_{max} = 4.120$, $\Theta_{min} = -3.589$, $\Omega_{max} = 3.548$, and $\Omega_{min} = -3.777$.

4.4. Effect of Darcy number

In this section, the influence of the porous medium coarseness ($10^{-6} \leqslant Da \leqslant 10^{3}$) on the double diffusion is investigated. The strip pitch and thermal Rayleigh number are maintained at $0.75H$ and 10^5, respectively. As Darcy number increases from 10^{-6} to 10^3 with upward mass transfer, the effect of the viscous forces accounted for in the Brinkman term on the flow velocity becomes significant. Observing from Fig. 11a, $Da = 10^{-6}$, the flow approaches stationary due to high hydraulic resistance imposed on the flow by low permeability medium. Heatlines and masslines demonstrate that the heat and solute are transported diffusively. As the Darcy number increases, porous medium increases viscous dissipation. Therefore, it is expected that as Da increases, the porous medium imposed less hydraulic resistance to the flow. As Da increases to 10^{-4}, the flow intensity increases, and consequently the concentration gradients at the walls are greater when the Brinkman term becomes significant. Continually increasing the Darcy number to 10^{-2}, as shown in Fig. 11c, the dynamic boundary layer becomes thinner when one observes the streamline patterns. The isotherms and concentration fields also have similar structures presented in Fig. 2b ($Da = 10^2$), which corresponds to the situation of fluid limit.

The effect of Darcy number on the overall heat and mass transfer rates, Nu and Sh are illustrated in Fig. 12 for the heat-transfer-driven flow ($N = 0$) and the solute-driven flow ($N = 10$). As the permeability of the porous medium Da is increased, the boundary frictional resistance becomes gradually less important and the fluid circulation within the enclosure is progressively enhanced. The viscous force enhances the velocity at high Darcy numbers. The results indicate that when Da is large enough, Nu and Sh tend asymptotically toward constant values that depend on the solutal Rayleigh numbers ($Ra_s = Ra_t LeN$). The limit $Da \to 0$ corresponds to a pure Darcy medium situation which has been studied recently by Zhao et al. [28] and Liu et al. [29]. As a result, Nu and Sh are observed to decrease considerably with decreasing Da toward the pure diffusion limit. This is expected since, in the limit of Da approaching to 0, the Brinkman model reduces to Darcy Law. Indeed, as the Darcy number is decreased, the boundary frictional resistance becomes progressively significant and adds to the bulk frictional drag induced by the solid matrix to slow the convection motion. Comparing Fig. 11a–c and Fig. 2b, it is found that the strength of the overall convective flow becomes weaker as the value of Da is made smaller.

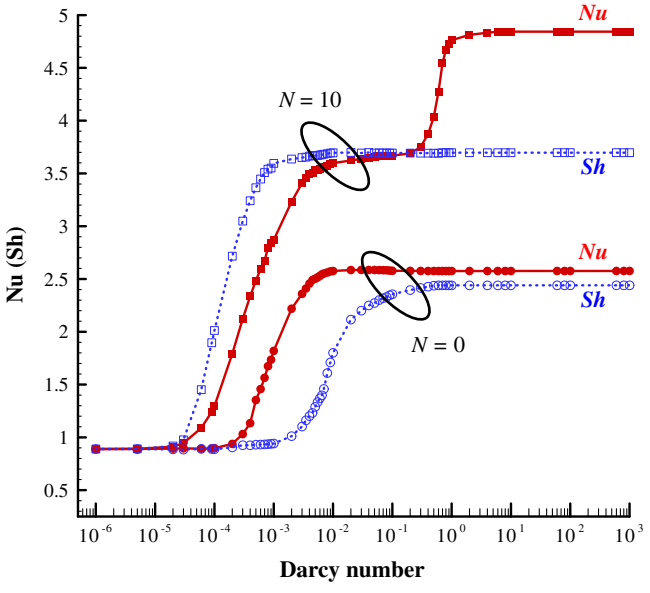

Fig. 12. Overall heat and mass transfer rates variation with permeability for different buoyancy ratios with upward mass transfer, $L_{ts} = 0.75H$, and $Ra_t = 10^5$.

5. Conclusions

Present study deals with double-diffusive natural convection in a horizontal porous enclosure saturated with gaseous pollutant (or moist air) of $Le \approx 0.8$, where discrete heat and moisture sources are attached to the bottom wall.

The obtained heatlines and masslines, for the combined heat and mass transfer problem under analysis, are shown to be a very effective way to visualize the paths followed by heat and moisture, through the porous layer. Visualization results thus provide more vigorous means to discuss the convective heat and mass transfer.

Multiplicity of linearly stable steady-states exists for supercritical natural convection in the enclosure filled with sparse porous medium ($Da = 10^2$). The existence of a multiplicity of steady-state solutions for the present numerical problem has been demonstrated numerically through the use of appropriate initial perturbations. In the regime that both thermal and concentration buoyancy forces are destabilizing, single and multiple cell convections take place, depending on the buoyancy ratio, thermal Rayleigh number and strip pitch. Solutal-dominated anti-clockwise flow ($N \gg 0$) can be sustained till N is lower than 0.2. The natural solution of multiple cells can be maintained at a smaller range of $0.6 < N < 1.4$. In the destabilizing and equal thermosolutal buoyant forces regime, for a given value of N the effects of both Ra_t and L_{ts} on the flow patterns have been investigated. For intermediate values of $1.2 \times 10^4 < Ra_t < 2.5 \times 10^4$, the existence of three possible solutions is demonstrated. For lower values of $Ra_t < 4 \times 10^3$, unique diffusion-dominated flow patterns are observed. The effect of strip pitch L_{ts} has been studied for the cases of unicellular and bicellular circulations. Three solutions, four solutions, and unique solution can be observed respectively for the ranges of $0 < L_{ts}/H < 0.2$, $0.2 < L_{ts}/H < 1.3$, and $L_{ts}/H > 1.3$. The associated overall heat and mass transfer rates are also obtained. It is this multiple transfer behaviors in the porous enclosure that gives to this gaseous double diffusion much interest and so high potential to apply in

building components where heat and moisture transfer simultaneously occurs.

At last, effect of Darcy number on the double-diffusive convection has also been examined for heat-transfer-driven flow and solutal-dominated flow. The main contributions of decreasing the Darcy number are predicted to be a flow retardation effect and diffuse transport of heat and mass in the enclosure.

Acknowledgements

This work was supported by the National Natural Science Foundation of China (No. 50578059). The constructive comments of the reviewers are also highly appreciated.

References

[1] J.S. Turner, Multi-component convection, Ann. Rev. Fluid Mech. 17 (1985) 11–44.
[2] R. Viskanta, T.L. Bergman, F.P. Incropera, Double diffusive natural convection, in: S. Kakac, W. Aung, R. Viskanta (Eds.), Natural Convection: Fundamentals and Applications, Hemisphere, Washington, DC, 1985, pp. 1075–1099.
[3] A. Bejan, Convection Heat Transfer, second ed., Wiley, New York, 1995, pp. 22, 505, 475.
[4] J.S. Turner, The behavior of a stable salinity gradient heated from below, J. Fluid Mech. 33 (1968) 183–200.
[5] H.K. Wee, R.B. Keey, M.J. Cunningham, Heat and moisture transfer by natural convection in a rectangular cavity, Int. J. Heat Mass Transfer 32 (1989) 1765–1778.
[6] F. Chen, C.F. Chen, Double-diffusive fingering convection in a porous medium, Int. J. Heat Mass Transfer 36 (1993) 793–807.
[7] O.V. Trevisan, A. Bejan, Natural convection with combined heat and mass transfer buoyancy effects in a porous medium, Int. J. Heat Mass Transfer 28 (1985) 1597–1611.
[8] O.V. Trevisan, A. Bejan, Mass and heat transfer by natural convection in a vertical slot filled with porous medium, Int. J. Heat Mass Transfer 29 (1986) 403–415.
[9] O.V. Trevisan, A. Bejan, Combined heat and mass transfer by natural convection in a vertical enclosure, ASME J. Heat Transfer 109 (1987) 104–112.
[10] T.F. Lin, C.C. Huang, T.S. Chang, Transient binary mixture natural convection in square enclosures, Int. J. Heat Mass Transfer 33 (1990) 287–299.
[11] C. Beghein, F. Haghighat, F. Allard, Numerical study of double-diffusive natural convection in a square cavity, Int. J. Heat Mass Transfer 35 (1992) 833–846.
[12] V.A.F. Costa, Double diffusive natural convection in a square enclosure with heat and mass diffusive walls, Int. J. Heat Mass Transfer 40 (1997) 4061–4071.
[13] V.A.F. Costa, Double-diffusive natural convection in parallelogrammic enclosures filled with fluid-saturated porous media, Int. J. Heat Mass Transfer 47 (2004) 2699–2714.
[14] V.A.F. Costa, Double-diffusive natural convection in parallelogrammic enclosures, Int. J. Heat Mass Transfer 47 (2004) 2913–2926.
[15] A.J. Chamkha, H. Al-Naser, Double-diffusive convection in an inclined porous enclosure with opposing temperature and concentration gradients, Int. J. Therm. Sci. 40 (2001) 227–244.
[16] A.J. Chamkha, Double-diffusive convection in a porous enclosure with cooperating temperature and concentration gradients and heat generation or absorption effects, Numer. Heat Transfer, Part A 41 (2002) 65–87.
[17] A.J. Chamkha, H. Al-Naser, Hydromagnetic double-diffusive convection in a rectangular enclosure with opposing temperature and concentration gradients, Int. J. Heat Mass Transfer 45 (2002) 2465–2483.
[18] A.J. Chamkha, H. Al-Naser, Hydromagnetic double-diffusive convection in a rectangular enclosure with uniform side heat and mass fluxes and opposing temperature and concentration gradients, Int. J. Therm. Sci. 41 (2002) 936–948.
[19] F.Y. Zhao, D. Liu, G.F. Tang, Application issues of the streamline, heatline and massline for conjugate heat and mass transfer, Int. J. Heat Mass Transfer 50 (2007) 320–334.
[20] J. Lee, M.T. Hyun, Y.S. Kang, Confined natural convection due to lateral heating in a stably stratified solution, Int. J. Heat Mass Transfer 33 (1990) 869–875.
[21] J.W. Lee, J.M. Hyun, Time-dependent double diffusion in a stably stratified fluid under lateral heating, Int. J. Heat Mass Transfer 34 (1991) 2409–2421.
[22] J.W. Lee, J.M. Hyun, Double-diffusive convection in a cavity under a vertical solutal gradient and a horizontal temperature gradient, Int. J. Heat Mass Transfer 34 (1991) 2423–2427.
[23] T.A. Newell, J.R. Hull, Depth sounding diagnostic measurement of salt gradient solar ponds, J. Solar Energy Eng. 107 (1985) 160–164.
[24] T.L. Bergman, A. Ungan, Experimental and numerical investigation of double-diffusive convection induced by a discrete heat source, Int. J. Heat Mass Transfer 29 (1986) 1695–1709.
[25] W. Chen, F.Y. Zhao, G.F. Tang, D. Liu, Transportation of indoor double diffusive mixed convection coupled with diffusion in solid walls, J. HV&AC 36 (2006) 12–18.
[26] F.Y. Zhao, D. Liu, G.F. Tang, Multiple steady flows in confined gaseous double diffusion with discrete thermosolutal sources, Phys. Fluids 19 (10) (2007) 107103.
[27] F.Y. Zhao, D. Liu, G.F. Tang, Natural convection in a porous enclosure with a partial heating and salting element, Int. J. Therm. Sci. (2007), doi:10.1016/j.ijthermalsci.2007.04.006.
[28] F.Y. Zhao, D. Liu, G.F. Tang, Free convection from one thermal and solute source in a confined porous medium, Transport Porous Media (2007), doi:10.1007/s11242-007-9106-7.
[29] D. Liu, F.Y. Zhao, G.F. Tang, Thermosolutal convection in a saturated porous enclosure with concentrated energy and solute sources, Energy Convers. Manage. 49 (2008) 16–31.
[30] T.J. Heindel, F.P. Incropera, S. Ramadhyani, Enhancement of natural convection heat transfer from an array of discrete heat sources, Int. J. Heat Mass Transfer 39 (1996) 479–490.
[31] S.K.W. Tou, C.P. Tso, X. Zhang, 3-D numerical analysis of natural convective liquid cooling of 3×3 heater array in rectangular enclosures, Int. J. Heat Mass Transfer 42 (1999) 3231–3244.
[32] S.K.W. Tou, X.F. Zhang, Three-dimensional numerical simulation of natural convection in an inclined liquid-filled enclosure with an array of discrete heaters, Int. J. Heat Mass Transfer 46 (2003) 127–138.
[33] C.P. Tso, L.F. Jin, S.K.W. Tou, X.F. Zhang, Flow pattern evolution in natural convection cooling from an array of discrete heat sources in a rectangular cavity at various orientations, Int. J. Heat Mass Transfer 47 (2004) 4061–4073.
[34] A.K. da Silva, S. Lorente, A. Bejan, Optimal distribution of discrete heat sources on a wall with natural convection, Int. J. Heat Mass Transfer 47 (2004) 203–214.
[35] A.K. da Silva, G. Lorenzini, A. Bejan, Distribution of heat sources in vertical open channels with natural convection, Int. J. Heat Mass Transfer 48 (2005) 1462–1469.
[36] L.F. Jin, S.K.W. Tou, C.P. Tou, Effects of rotation on natural convection cooling from three rows of heat sources in a rectangular cavity, Int. J. Heat Mass Transfer 48 (2005) 3982–3994.
[37] Y.L. He, W.W. Yang, W.Q. Tao, Three-dimensional numerical study of natural convective heat transfer of liquid in a cubic enclosure, Numer. Heat Transfer, Part A 47 (2005) 917–934.
[38] F.Y. Zhao, D. Liu, G.F. Tang, Resonant response of fluid flow subjected to discrete heating elements, Energy Convers. Manage. 48 (2007) 2461–2472.
[39] F.Y. Zhao, D. Liu, G.F. Tang, Conjugate heat transfer in square enclosures, Heat Mass Transfer 43 (2007) 907–922.

[40] F.Y. Zhao, G.F. Tang, D. Liu, Conjugate natural convection in enclosures with external and internal heat sources, Int. J. Eng. Sci. 44 (2006) 148–165.

[41] D. Liu, F.Y. Zhao, G.F. Tang, Conjugate heat transfer in an enclosure with a centered conducting body imposed sinusoidal temperature profiles on one side, Numer. Heat Transfer, Part A 53 (2) (2008) 204–223.

[42] S.V. Patankar, Numerical Heat Transfer and Fluid Flow, Hemisphere, Washington, DC, 1980.

[43] T. Hayase, J.A.C. Humphrey, R. Greif, A consistently formulated QUICK scheme for fast and stable convergence using finite-volume iterative calculation procedure, J. Comput. Phys. 98 (1992) 108–118.